 CMES, vol.83, no.3, pp.311-351, 2012

Local Moving Least Square - One-Dimensional IRBFN Technique: Part II - Unsteady Incompressible Viscous Flows

D. Ngo-Cong[1,2], N. Mai-Duy[1], W. Karunasena[2] and T. Tran-Cong[1,3]

Abstract: In this study, local moving least square - one dimensional integrated radial basis function network (LMLS-1D-IRBFN) method is presented and demonstrated with the solution of time-dependent problems such as Burgers' equation, unsteady flow past a square cylinder in a horizontal channel and unsteady flow past a circular cylinder. The present method makes use of the partition of unity concept to combine the moving least square (MLS) and one-dimensional integrated radial basis function network (1D-IRBFN) techniques in a new approach. This approach offers the same order of accuracy as its global counterpart, the 1D-IRBFN method, while the system matrix is more sparse than that of the 1D-IRBFN, which helps reduce the computational cost significantly. For fluid flow problems, the diffusion terms are discretised by using LMLS-1D-IRBFN method, while the convection terms are explicitly calculated by using 1D-IRBFN method. The present numerical procedure is combined with a domain decomposition technique to handle large-scale problems. The numerical results obtained are in good agreement with other published results in the literature.

Keywords: Unsteady flow, Burgers' equation, square cylinder, circular cylinder, moving least square, integrated radial basis function, domain decomposition.

1 Introduction

Time-dependent analysis plays a very important role in the design of diverse engineering products and systems, e.g. in aerospace, automotive, marine and civil applications. In this paper, a new efficient numerical method is developed for

[1] Computational Engineering and Science Research Centre, Faculty of Engineering and Surveying, The University of Southern Queensland, Toowoomba, QLD 4350, Australia.
[2] Centre of Excellence in Engineered Fibre Composites, Faculty of Engineering and Surveying, The University of Southern Queensland, Toowoomba, QLD 4350, Australia.
[3] Corresponding author, Email: trancong@usq.edu.au.

the solution of time-dependent problems and illustrated with examples such as the well-known Burgers' equation, unsteady flows past a square cylinder in a horizontal channel, and unsteady flows past a circular cylinder. Burgers' equation has been studied by many authors to verify their proposed numerical methods because it is the simplest nonlinear equation that includes convection and dissipation terms. Caldwell, Wanless, and Cook (1987) presented a moving node finite element method to obtain a solution of Burgers' equation under different prescribed conditions. Iskander and Mohsen (1992) devised new algorithms based on a combination of linearization and splitting-up for solving this equation. Hon and Mao (1998) solved Burgers' equation using multiquadric (MQ) for spatial discretisation and a low order explicit finite difference scheme for temporal discretisation. Their numerical results indicated that the major numerical error is from the time integration instead of the MQ spatial approximation. Hassanien, Salama, and Hosham (2005) developed fourth-order finite difference method based on two-level three-point finite difference for solving Burgers' equation. Hashemian and Shodja (2008) proposed a gradient reproducing kernel particle method (GRKPM) for spatial discretisation of Burgers' equation to obtain equivalent nonlinear ordinary differential equations which are then discretised in time by the Gear's method. Hosseini and Hashemi (2011) presented a local-RBF meshless method for solving Burgers' equation with different initial and boundary conditions.

Flows past a circular cylinder have been extensively studied by many researchers to verify their new numerical methods for irregular domains. There is no singularity on a circular cylinder surface and the flow field behind the cylinder contains a variety of fluid dynamic phenomena, which makes the problem interesting as a benchmark. Cheng, Liu, and Lam (2001) applied a discrete vortex method to investigate an unsteady flow past a rotationally oscillating circular cylinder for different values of oscillating amplitude and frequency at a Reynolds number of 200. Based on the numerical results obtained, they provided a map of lock-on and non-lock-on regions which helps to classify the different vortex structure in the wake with respect to the oscillating amplitude and frequency of the cylinder.

For the problem of flow past a square cylinder, singularities occur at the corners of the square cylinder, which poses some challenges in terms of accurate determination of such singularities. In order to obtain a convergent solution, very dense grids are usually generated near the singularities. Davis and Moore (1982) studied unsteady flow past a rectangular cylinder using finite difference method (FDM) with third-order upwind differencing for convection, standard central scheme for diffusion terms and a Leith-type scheme for time integration. Zaki, Sen, and el Hak (1994) conducted a numerical study of flow past a fixed square cylinder at various angles of incidence for Reynolds numbers up to 250. Their numerical simula-

tion was based on the stream function-vorticity formulation of the Navier-Stokes equation together with a single-valued pressure condition to make the problem well-posed. Sohankar, Norberg, and Davidson (1998) presented calculations of unsteady 2-D flows around a square cylinder at different angles of incidence using an incompressible SIMPLEC finite volume code with a non-staggered grid arrangement. The convective terms were discretised using the third-order QUICK differencing scheme, while the diffusive terms were discretised using central differences. Breuer, Bernsdorf, Zeiser, and Durst (2000) investigated a confined flow around a square cylinder in a channel with blockage ratio of $1/8$ by a lattice-Boltzmann automata (LBA) and a finite volume method (FVM). Turki, Abbassi, and Nasrallah (2003) studied an unsteady flow and heat transfer characteristics in a channel with a heated square cylinder using a control volume finite element method (CVFEM) adapted to a staggered grid. In their work, the influences of blockage ratio, Reynolds number and Richardson number on the flow pattern were investigated. Berrone and Marro (2009) applied a space-time adaptive method to solve unsteady flow problems including flows over backward facing step and flows past a square cylinder in a channel. Moussaoui, Jami, Mezrhab, and Naji (2010) simulated a 2-D flow and heat transfer in a horizontal channel obstructed by an inclined square cylinder using a hybrid scheme with lattice Boltzmann method to determine the velocity field and FDM to solve the energy equation.

Dhiman, Chhabra, and Eswaran (2005) investigated influences of blockage ratio, Prandtl number and Peclet number on the flow and heat transfer characteristics of an isolated square cylinder confined in a channel in a 2-D steady flow regime ($1 \leq Re \leq 45$) using semi-explicit FEM on a non-uniform Cartesian grid. The third order QUICK scheme was used to discretise the convection terms, while the second-order central difference scheme was used to discretise the diffusion terms. The semi-explicit FEM was also applied to a steady laminar mixed convection flow across a heated square cylinder in a channel [Dhiman, Chhabra, and Eswaran (2008)]. Sahu, Chhabra, and Eswaran (2010) conducted a study of 2-D unsteady flow of power-law fluids past a square cylinder confined in a channel for different values of Reynolds number ($60 \leq Re \leq 160$), blockage ratio ($\beta_0 = 1/6, 1/4$ and $1/2$) and power-law flow behaviour index ($0.5 \leq n \leq 1.8$) using the semi-explicit FEM. Bouaziz, Kessentini, and Turki (2010) employed a control volume finite element method (CVFEM) adapted to the staggered grid to study an unsteady laminar flow and heat transfer of power-law fluids in 2-D horizontal plane channel with a heated square cylinder.

In the past decades, some mesh-free and local RBF-based methods have been developed for solving fluid flow problems. Shu, Ding, and Yeo (2003) presented a local RBF-based differential quadrature method (local RBF-DQ) for a simulation

of natural convection in a square cavity. In their study, three layers of orthogonal grid near and including the boundary were generated for imposing the Neumann condition of temperature and the vorticity on the wall. The derivatives of the field variables in the boundary conditions were then discretised by the conventional one-sided second order finite difference scheme. The local RBF-DQ method was also employed for solving several cases of incompressible flows including a driven-cavity flow, flow past a cylinder, and flow around two staggered circular cylinders [Shu, Ding, and Yeo (2005)]. Ding, Shu, Yeo, and Xu (2007) presented the mesh-free least square-based finite difference (MLSFD) method to simulate a flow field around two circular cylinders arranged in tandem and side-by-side. Vertnik and Šarler (2006) presented an explicit local RBF collocation method for diffusion problems. Sanyasiraju and Chandhini (2008) developed a local RBF based gridfree scheme for unsteady incompressible viscous flows in terms of primitive variables. Chen, Hu, and Hu (2008) employed a partition of unity concept [Babuŝka and Melenk (1997)] to combine the reproducing kernel and RBF approximations to yield a local approximation that enjoys the exponential convergence of RBF and improves the conditioning of the discrete system. Le, Rabczuk, Mai-Duy, and Tran-Cong (2010) proposed a locally supported moving IRBFN-based meshless method for solving various problems including heat transfer, elasticity of both compressible and incompressible materials, and linear static crack problems.

Another approach for solving PDEs is the so-called Cartesian grid method where the governing equations are discretised with a fixed Cartesian grid. This approach significantly reduces the grid generation cost and has a great potential over the conventional body-fitted methods when solving problems with moving boundary and complicated geometry. Udaykumar, Mittal, Rampunggoon, and Khanna (2001) presented a Cartesian grid method for computing fluid flows with complex immersed and moving boundaries. The incompressible Navier-Stokes equations are discretised using a second-order FVM, and second-order fractional-step scheme is employed for time integration. Russell and Wang (2003) presented a Cartesian grid method for solving 2-D incompressible viscous flows around multiple moving objects based on stream function-vorticity formulation. Zheng and Zhang (2008) employed an immersed-boundary method to predict the flow structure around a transversely oscillating cylinder. The influences of oscillating frequency on the drag and lift acting on the cylinder were investigated.

As an alternative to the conventional differentiated radial basis function network (DRBFN) method [Kansa (1990)], Mai-Duy and Tran-Cong (2001a) proposed the use of integration to construct the RBFN expressions (the IRBFN method) for the approximation of a function and its derivatives and for the solution of PDEs. Numerical results showed that the IRBFN method achieves superior accuracy [Mai-

Duy and Tran-Cong (2001a); Mai-Duy and Tran-Cong (2001b)]. A one-dimensional integrated radial basis function network (1D-IRBFN) collocation method for the solution of second- and fourth-order PDEs was presented by Mai-Duy and Tanner (2007). Along grid lines, 1D-IRBFN are constructed to satisfy the governing differential equations with boundary conditions in an exact manner. In the 1D-IRBFN method, the Cartesian grids were used to discretise both rectangular and non-rectangular problem domains. The 1D-IRBFN method is much more efficient than the original IRBFN method reported by Mai-Duy and Tran-Cong (2001a). Le-Cao, Mai-Duy, Tran, and Tran-Cong (2011) employed the 1D-IRBFN method to simulate unsymmetrical flows of a Newtonian fluid in multiply-connected domains using the stream-function and temperature formulation. Ngo-Cong, Mai-Duy, Karunasena, and Tran-Cong (2011) extended this method to investigate free vibration of composite laminated plates based on first-order shear deformation theory. Ngo-Cong, Mai-Duy, Karunasena, and Tran-Cong (2012) proposed a local moving least square - one dimensional integrated radial basis function network method (LMLS-1D-IRBFN) for simulating 2-D steady incompressible viscous flows in terms of stream function and vorticity. In the present study, we further extend the LMLS-1D-IRBFN method for solving time-dependent problems and demonstrate the new procedure with the simulation of Burgers' equation, unsteady flows past a square cylinder in a horizontal channel, and unsteady flows past a circular cylinder. The present numerical procedure is combined with a domain decomposition technique to handle large-scale problems.

The paper is organised as follows. The LMLS-1D-IRBFN method is presented in Section 2. The governing equations for incompressible viscous flows are given in Section 3. Several numerical examples are investigated using the proposed method in Section 4. Section 5 concludes the paper.

2 Local moving least square - one dimensional integrated radial basis function network technique

A schematic outline of the LMLS-1D-IRBFN method is depicted in Fig. 1. The proposed method with 3-node support domains ($n = 3$) and 5-node local 1D-IRBF networks ($n_s = 5$) is presented here. On an x-grid line $[l]$, a global interpolant for the field variable at a grid point x_i is sought in the form

$$u(x_i) = \sum_{j=1}^{n} \bar{\phi}_j(x_i) u^{[j]}(x_i), \tag{1}$$

where $\left\{\bar{\phi}_j\right\}_{j=1}^{n}$ is a set of the partition of unity functions constructed using MLS approximants [Liu (2003)]; $u^{[j]}(x_i)$ the nodal function value obtained from a local

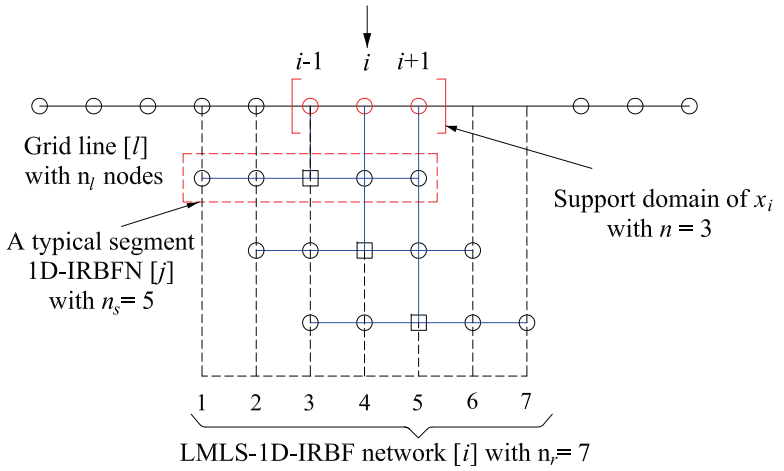

Figure 1: LMLS-1D-IRBFN scheme, □ a typical [j] node.

interpolant represented by a 1D-IRBF network [j]; n the number of nodes in the support domain of x_i. In (1), MLS approximants are presently based on linear polynomials, which are defined in terms of 1 and x. It is noted that the MLS shape functions possess a so-called partition of unity properties as follows.

$$\sum_{j=1}^{n} \bar{\phi}_j(x) = 1. \tag{2}$$

Relevant derivatives of u at x_i can be obtained by differentiating (1)

$$\frac{\partial u(x_i)}{\partial x} = \sum_{j=1}^{n} \left(\frac{\partial \bar{\phi}_j(x_i)}{\partial x} u^{[j]}(x_i) + \bar{\phi}_j(x_i) \frac{\partial u^{[j]}(x_i)}{\partial x} \right), \tag{3}$$

$$\frac{\partial^2 u(x_i)}{\partial x^2} = \sum_{j=1}^{n} \left(\frac{\partial^2 \bar{\phi}_j(x_i)}{\partial x^2} u^{[j]}(x_i) + 2 \frac{\partial \bar{\phi}_j(x_i)}{\partial x} \frac{\partial u^{[j]}(x_i)}{\partial x} + \bar{\phi}_j(x_i) \frac{\partial^2 u^{[j]}(x_i)}{\partial x^2} \right), \tag{4}$$

where the values $u^{[j]}(x_i), \partial u^{[j]}(x_i)/\partial x$ and $\partial^2 u^{[j]}(x_i)/\partial x^2$ are calculated from 1D-IRBFN networks with n_s nodes.

Full details of the LMLS-1D-IRBFN method can be found in [Ngo-Cong, Mai-Duy, Karunasena, and Tran-Cong (2012)].

3 Governing equations for 2-D unsteady incompressible viscous flows

The governing equations for 2-D incompressible viscous flows written in terms of stream function ψ and vorticity ω are given by

$$\frac{\partial^2\psi}{\partial x^2}+\frac{\partial^2\psi}{\partial y^2}=-\omega, \tag{5}$$

$$\frac{1}{Re}\left(\frac{\partial^2\omega}{\partial x^2}+\frac{\partial^2\omega}{\partial y^2}\right)=\frac{\partial\omega}{\partial t}+\left(\frac{\partial\psi}{\partial y}\frac{\partial\omega}{\partial x}-\frac{\partial\psi}{\partial x}\frac{\partial\omega}{\partial y}\right), \tag{6}$$

where Re is the Reynolds number, t the time, and $(x,y)^T$ the position vector. The x and y components of the velocity vector can be defined in terms of the stream function as

$$u=\frac{\partial\psi}{\partial y}, \tag{7}$$

$$v=-\frac{\partial\psi}{\partial x}. \tag{8}$$

The computational boundary conditions for vorticity can be computed as

$$\omega_w=-\left(\frac{\partial^2\psi_w}{\partial x^2}+\frac{\partial^2\psi_w}{\partial y^2}\right) \tag{9}$$

where the subscript w is used to denote quantities on the boundary. For curved boundaries, a formula reported in [Le-Cao, Mai-Duy, and Tran-Cong (2009)] is employed here to derive the vorticity boundary conditions at boundary points on x- and y-grid lines as follows.

$$\omega_w^{(x)}=-\left[1+\left(\frac{t_x}{t_y}\right)^2\right]\frac{\partial^2\psi_w}{\partial x^2}-q_y, \tag{10}$$

$$\omega_w^{(y)}=-\left[1+\left(\frac{t_y}{t_x}\right)^2\right]\frac{\partial^2\psi_w}{\partial y^2}-q_x, \tag{11}$$

where q_x and q_y are known quantities defined by

$$q_x=-\frac{t_y}{t_x^2}\frac{\partial^2\psi_w}{\partial y\partial s}+\frac{1}{t_x}\frac{\partial^2\psi_w}{\partial x\partial s}, \tag{12}$$

$$q_y=-\frac{t_x}{t_y^2}\frac{\partial^2\psi_w}{\partial x\partial s}+\frac{1}{t_y}\frac{\partial^2\psi_w}{\partial y\partial s}, \tag{13}$$

in which $t_x=\partial x/\partial s, t_y=\partial y/\partial s$ and s is the direction tangential to the curved surface.

Boundary conditions for stream function are specified in the following examples.

4 Numerical results and discussion

Several time-dependent problems are considered in this section to study the performance of the present numerical procedure. The domains of interest are discretised using Cartesian grids. The simple Euler scheme is used for time integration. For Burgers' equation, the LMLS-1D-IRBFN method is employed to discretise both diffusion and convection terms. For fluid flow problems, the LMLS-1D-IRBFN is used to discretise the diffusion terms while the convection terms are explicitly calculated by using the 1D-IRBFN technique. A domain decomposition technique is employed for solving the fluid flow problems. By using the LMLS-1D-IRBFN method to discretise the left hand side of governing equations and the LU decomposition technique to solve the resultant sparse system of simultaneous equations, the computational cost and data storage requirements are reduced.

4.1 Example 1: Burgers' equation

The present numerical method is first verified through the solution of Burgers' equation as follows.

$$\frac{\partial u}{\partial t}+u\frac{\partial u}{\partial x}=\frac{1}{Re}\frac{\partial^2 u}{\partial x^2}. \tag{14}$$

The diffusion and convection terms in Equation (14) are discretised on a uniform grid using LMLS-1D-IRBFN method implicitly and explicitly, respectively.

4.1.1 Approximation of shock wave propagation

Consider the Burgers' equation (14) defined on a segment $0 \leq x \leq 1, t \geq 0$ and subject to Dirichlet boundary conditions. The initial and boundary conditions can be calculated from the following analytical solution [Hassanien, Salama, and Hosham (2005); Hosseini and Hashemi (2011)]

$$u_E(x,t)=\frac{[\alpha_0+\mu_0+(\mu_0-\alpha_0)\exp(\eta)]}{1+\exp(\eta)}, \tag{15}$$

where $\eta=\alpha_0 Re(x-\mu_0 t-\beta_0)$, $\alpha_0=0.4, \beta_0=0.125, \mu_0=0.6, Re=100$.

Tab. 1 shows the comparison among the numerical results of LMLS-1D-IRBFN and 1D-IRBFN methods and the exact solution at time $t=1.0$ for several time step sizes and using a grid of 61. It can be seen that the accuracy is greatly improved by reducing the time step. Grid convergence studies for both methods with the same time step of 10^{-3} are given in Tab. 2. The numerical results show that the accuracy is not improved much with increasing grid density for both methods, which

Table 1: Burgers' equations, approximation of shock wave propagation: comparison of numerical results and exact solution at $t = 1.0$ for $Re = 100$ and several time step sizes, using a grid of 61. (1) 1D-IRBFN, (2) LMLS-1D-IRBFN

		$dt = 10^{-2}$		$dt = 10^{-3}$		$dt = 10^{-4}$	
x	Exact	(1)	(2)	(1)	(2)	(1)	(2)
0.000	1.0000	1.0000	1.0000	1.0000	1.0000	1.0000	1.0000
0.056	1.0000	1.0000	1.0000	1.0000	1.0000	1.0000	1.0000
0.111	1.0000	1.0000	1.0000	1.0000	1.0000	1.0000	1.0000
0.167	1.0000	1.0000	1.0000	1.0000	1.0000	1.0000	1.0000
0.222	0.9998	1.0000	1.0000	0.9999	0.9998	0.9998	0.9998
0.278	0.9978	1.0000	0.9999	0.9983	0.9982	0.9980	0.9979
0.333	0.9801	0.9991	0.9988	0.9829	0.9831	0.9808	0.9810
0.389	0.8473	0.9153	0.9145	0.8545	0.8547	0.8495	0.8496
0.444	0.4518	0.4516	0.4526	0.4533	0.4539	0.4533	0.4539
0.500	0.2379	0.2387	0.2383	0.2382	0.2379	0.2381	0.2379
0.556	0.2043	0.2050	0.2050	0.2044	0.2044	0.2043	0.2043
0.611	0.2005	0.2006	0.2006	0.2005	0.2005	0.2005	0.2005
0.667	0.2001	0.2001	0.2001	0.2001	0.2001	0.2001	0.2001
0.722	0.2000	0.2000	0.2000	0.2000	0.2000	0.2000	0.2000
0.778	0.2000	0.2000	0.2000	0.2000	0.2000	0.2000	0.2000
0.833	0.2000	0.2000	0.2000	0.2000	0.2000	0.2000	0.2000
0.889	0.2000	0.2000	0.2000	0.2000	0.2000	0.2000	0.2000
0.944	0.2000	0.2000	0.2000	0.2000	0.2000	0.2000	0.2000
1.000	0.2000	0.2000	0.2000	0.2000	0.2000	0.2000	0.2000
Ne		2.45E-02	2.42E-02	2.75E-03	2.86E-03	9.51E-04	1.12E-03

indicates that the major numerical error is not from the LMLS-1D-IRBFN and 1D-IRBFN spatial approximation, but from the temporal discretisation. It is noted that the LMLS-1D-IRBFN method offers the same level of accuracy as the 1D-IRBFN method.

4.1.2 Sinusoidal initial condition

Consider the Burgers' Equation (14) defined on a segment $0 \leq x \leq 1, t \geq 0$ and subject to the following Dirichlet boundary conditions and initial condition.

$$u(0,t) = u(1,t) = 0, \quad t > 0, \tag{16}$$

$$u(x,0) = \sin \pi x, \qquad 0 \leq x \leq 1. \tag{17}$$

Table 2: Burgers' equations, approximation of shock wave propagation: grid convergence study of numerical results for $Re = 100, t = 1.0$, and $\Delta t = 10^{-3}$. (1) 1D-IRBFN, (2) LMLS-1D-IRBFN

		$n_x = 41$		$n_x = 61$		$n_x = 81$	
x	Exact	(1)	(2)	(1)	(2)	(1)	(2)
0.000	1.0000	1.0000	1.0000	1.0000	1.0000	1.0000	1.0000
0.056	1.0000	1.0000	1.0000	1.0000	1.0000	1.0000	1.0000
0.111	1.0000	1.0000	1.0000	1.0000	1.0000	1.0000	1.0000
0.167	1.0000	1.0000	1.0000	1.0000	1.0000	1.0000	1.0000
0.222	0.9998	0.9999	0.9998	0.9999	0.9998	0.9999	0.9998
0.278	0.9978	0.9983	0.9979	0.9983	0.9982	0.9983	0.9983
0.333	0.9801	0.9829	0.9848	0.9829	0.9831	0.9829	0.9829
0.389	0.8473	0.8546	0.8554	0.8545	0.8547	0.8545	0.8546
0.444	0.4518	0.4534	0.4552	0.4533	0.4539	0.4533	0.4535
0.500	0.2379	0.2381	0.2372	0.2382	0.2379	0.2382	0.2381
0.556	0.2043	0.2044	0.2043	0.2044	0.2044	0.2044	0.2044
0.611	0.2005	0.2005	0.2005	0.2005	0.2005	0.2005	0.2005
0.667	0.2001	0.2001	0.2001	0.2001	0.2001	0.2001	0.2001
0.722	0.2000	0.2000	0.2000	0.2000	0.2000	0.2000	0.2000
0.778	0.2000	0.2000	0.2000	0.2000	0.2000	0.2000	0.2000
0.833	0.2000	0.2000	0.2000	0.2000	0.2000	0.2000	0.2000
0.889	0.2000	0.2000	0.2000	0.2000	0.2000	0.2000	0.2000
0.944	0.2000	0.2000	0.2000	0.2000	0.2000	0.2000	0.2000
1.000	0.2000	0.2000	0.2000	0.2000	0.2000	0.2000	0.2000
Ne		2.78E-03	3.48E-03	2.75E-03	2.86E-03	2.75E-03	2.78E-03

The corresponding analytical solution was found by Cole (1951) as follows.

$$u_E(x,t) = \frac{2\pi\varepsilon \sum_{j=1}^{\infty} j k_j \sin(j\pi x)\exp(-j^2\pi^2\varepsilon t)}{k_0 + \sum_{j=1}^{\infty} k_j \cos(j\pi x)\exp(-j^2\pi^2\varepsilon t)}, \tag{18}$$

where $\varepsilon = 1/\mathrm{Re}$, $k_0 = \int_0^1 \exp\left(-1-\cos\pi x/2\pi\varepsilon\right) dx$, and

$k_j = 2\int_0^1 \cos(j\pi x)\exp\left(-1-\cos\pi x/2\pi\varepsilon\right) dx.$

Tab. 3 presents the numerical results at several positions x and times t for Reynolds number of 10 and several grid sizes in comparison with the exact solution and the numerical results of Hosseini and Hashemi (2011) who used a local-RBF collocation for spatial discretisation and the explicit Euler scheme for time discretisation,

Table 3: Burgers' equations, sinusoidal initial condition: comparison among the numerical results of LMLS-1D-IRBFN and Local-RBF [Hosseini and Hashemi (2011)] and the analytical solution for $Re = 10$, $\Delta t = 10^{-3}$.

			$n_x = 9$	$n_x = 33$		$n_x = 57$		$n_x = 81$	
x	t	Exact	Present	Local-RBF	Present	Local-RBF	Present	Local-RBF	Present
0.25	0.4	0.30889	0.30820	0.30817	0.30838	0.30821	0.30838	0.30862	0.30839
	0.6	0.24074	0.24025	0.24026	0.24040	0.24030	0.24040	0.24059	0.24040
	0.8	0.19568	0.19556	0.19533	0.19543	0.19537	0.19543	0.19560	0.19543
	1.0	0.16256	0.16291	0.16230	0.16238	0.16234	0.16238	0.16253	0.16238
	3.0	0.02720	0.02762	0.02714	0.02720	0.02716	0.02720	0.02723	0.02720
0.50	0.4	0.56963	0.57036	0.56861	0.56896	0.56867	0.56896	0.56929	0.56896
	0.6	0.44721	0.44865	0.44643	0.44670	0.44651	0.44669	0.44701	0.44669
	0.8	0.35924	0.36150	0.35863	0.35886	0.35871	0.35885	0.35913	0.35885
	1.0	0.29192	0.29463	0.29142	0.29163	0.29150	0.29162	0.29187	0.29162
	3.0	0.04021	0.04081	0.04011	0.04020	0.04015	0.04020	0.04025	0.04020
0.75	0.4	0.62544	0.62926	0.62486	0.62515	0.62496	0.62511	0.62540	0.62511
	0.6	0.48721	0.49318	0.48646	0.48695	0.48658	0.48691	0.48712	0.48691
	0.8	0.37392	0.37992	0.37322	0.37371	0.37333	0.37369	0.37385	0.37369
	1.0	0.28747	0.29251	0.28688	0.28732	0.28698	0.28731	0.28744	0.28731
	3.0	0.02977	0.03021	0.02970	0.02977	0.02973	0.02977	0.02981	0.02977

Table 4: Burgers' equations, sinusoidal initial condition: comparison among the numerical results of LMLS-1D-IRBFN and Local-RBF [Hosseini and Hashemi (2011)] and the analytical solution for $Re = 100$, $\Delta t = 10^{-3}$.

			$n_x = 9$	$n_x = 33$		$n_x = 57$		$n_x = 81$	
x	t	Exact	Present	Local-RBF	Present	Local-RBF	Present	Local-RBF	Present
0.25	0.4	0.34191	0.33414	0.33395	0.34114	0.33396	0.34114	0.33794	0.34114
	0.6	0.26896	0.26353	0.26328	0.26841	0.26328	0.26841	0.26613	0.26841
	0.8	0.22148	0.21759	0.21722	0.22107	0.21723	0.22107	0.21936	0.22107
	1.0	0.18819	0.18523	0.18488	0.18787	0.18489	0.18787	0.18655	0.18787
	3.0	0.07511	0.07416	0.07438	0.07504	0.07438	0.07504	0.07476	0.07504
0.50	0.4	0.66071	0.64995	0.64907	0.65961	0.64908	0.65961	0.65496	0.65961
	0.6	0.52942	0.51822	0.51971	0.52848	0.51972	0.52849	0.52461	0.52849
	0.8	0.43914	0.42785	0.43139	0.43839	0.43140	0.43839	0.43530	0.43839
	1.0	0.37442	0.36512	0.36820	0.37381	0.36821	0.37381	0.37134	0.37381
	3.0	0.15018	0.14802	0.14872	0.15003	0.14873	0.15004	0.14947	0.15004
0.75	0.4	0.91026	0.85640	0.90742	0.91011	0.90749	0.91014	0.90905	0.91015
	0.6	0.76724	0.65947	0.75810	0.76643	0.75814	0.76643	0.76282	0.76643
	0.8	0.64740	0.55693	0.63810	0.64651	0.63812	0.64652	0.64284	0.64652
	1.0	0.55605	0.48796	0.54787	0.55524	0.54789	0.55527	0.55202	0.55527
	3.0	0.22481	0.20834	0.22261	0.22449	0.22265	0.22459	0.22376	0.22459

Table 5: Burgers' equations, sinusoidal initial condition: comparison among numerical results and exact solution for $Re = 10000$, $\Delta t = 10^{-4}$, using a grid of 301.

x	Exact	Caldwell, Wanless and Cook (1987)	Iskander and Mohsen (1992)	Hon and Mao (1998)	Present
0.056	0.0422	0.0422	0.0419	0.0424	0.0421
0.111	0.0843	0.0844	0.0839	0.0843	0.0842
0.167	0.1263	0.1266	0.1253	0.1263	0.1263
0.222	0.1684	0.1687	0.1692	0.1684	0.1683
0.278	0.2103	0.2108	0.2034	0.2103	0.2103
0.333	0.2522	0.2527	0.2666	0.2522	0.2521
0.389	0.2939	0.2946	0.2527	0.2939	0.2939
0.444	0.3355	0.3362	0.3966	0.3355	0.3355
0.500	0.3769	0.3778	0.2350	0.3769	0.3769
0.556	0.4182	0.4191	0.5480	0.4182	0.4182
0.611	0.4592	0.4601	0.2578	0.4592	0.4592
0.667	0.5000	0.5009	0.6049	0.4999	0.4999
0.722	0.5404	0.5414	0.6014	0.5404	0.5404
0.778	0.5806	0.5816	0.4630	0.5802	0.5805
0.833	0.6203	0.6213	0.7011	0.6201	0.6202
0.889	0.6596	0.6605	0.6717	0.6600	0.6595
0.944	0.6983	0.6992	0.7261	0.6957	0.6982

Table 6: Burgers' equations, sinusoidal initial condition: comparison of numerical results for $Re = 10000$, $\Delta t = 10^{-4}$, using a grid of 301.

x	Hassanien, Salama and Hosham (2005)	Hashemian and Shodja (2008)	Hosseini and Hashemi (2011)	Present
0.050	0.0379	0.0379	0.0379	0.0379
0.110	0.0834	0.0834	0.0833	0.0834
0.160	0.1213	0.1213	0.1212	0.1213
0.220	0.1667	0.1667	0.1666	0.1667
0.270	0.2044	0.2044	0.2044	0.2044
0.330	0.2469	0.2497	0.2496	0.2496
0.380	0.2872	0.2872	0.2871	0.2872
0.440	0.3322	0.3322	0.3321	0.3322
0.500	0.3769	0.3769	0.3768	0.3769
0.550	0.4140	0.4141	0.4140	0.4140
0.610	0.4584	0.4584	0.4583	0.4583
0.660	0.4951	0.4951	0.4950	0.4950
0.720	0.5388	0.5388	0.5387	0.5388
0.770	0.5749	0.5749	0.5748	0.5749
0.830	0.6179	0.6179	0.6178	0.6179
0.880	0.6533	0.6533	0.6530	0.6532
0.940	0.6952	0.6952	0.6890	0.6941

while the corresponding comparison for the case of Reynolds number of 100 is given in Tab. 4. For the purpose of comparison, the same time step is taken to be 10^{-3} in these cases. It can be seen that the present numerical results are slightly more accurate than those of the local-RBF in general.

The numerical results for the case of a large Reynolds number of 10000 at time $t = 1.0$ are described in Tabs. 5 and 6 using the same grid size of 301 and the same time step of 10^{-4} as reported in [Hosseini and Hashemi (2011)]. Tab. 5 gives the numerical results at a uniform grid with a grid spacing of $1/8$ in comparison with the exact solution and the results of other authors, while the corresponding comparison of numerical results at the same grid positions as reported in [Hassanien, Salama, and Hosham (2005); Hashemian and Shodja (2008); Hosseini and Hashemi (2011)] are provided in Tab. 6. Those comparisons show that the present numerical results are in good agreement with the exact and other numerical method solutions.

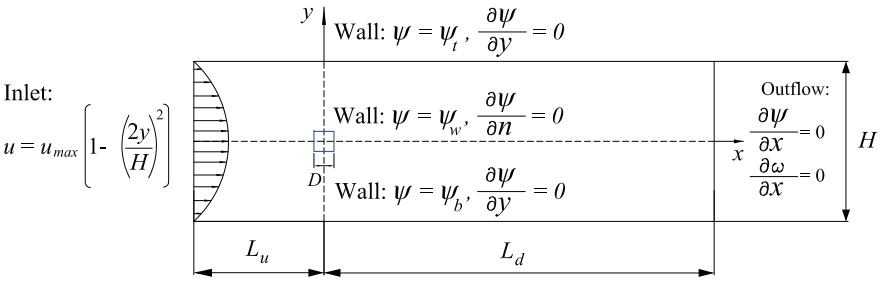

Figure 2: Flow past a square cylinder in a channel: geometry and boundary conditions. The blockage ratio is defined as $\beta_0 = D/H$. Note that computational boundary conditions for vorticity are determined by Equation (9).

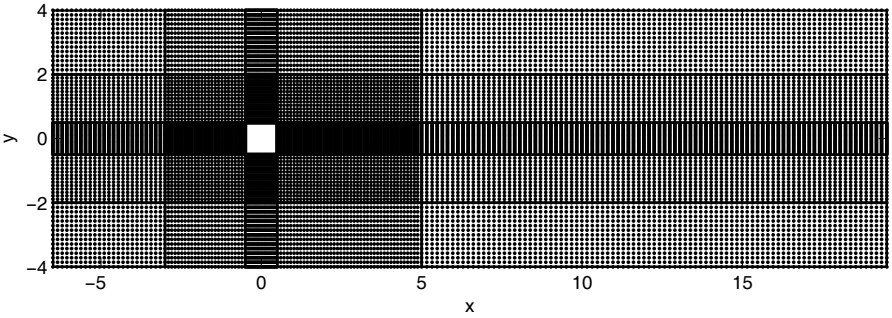

Figure 3: Flow past a square cylinder in a channel: grid configuration.

4.2 Example 2: Steady and unsteady flows past a square cylinder in a horizontal channel

The steady and unsteady flows past a square cylinder in a horizontal channel are considered here. The present LMLS-1D-IRBFN method is used for discretisation of diffusion terms implicitly, while the 1D-IRBFN method is employed to calculate the convection terms explicitly. The problem geometry and boundary conditions are described in Fig. 2. Note that computational boundary conditions for vorticity are determined by Equation (9). The distances from the inlet and outlet to the center of the square cylinder are taken to be $L_u = 6.5D$ and $L_d = 19.5D$, respectively, where D is the side length of the square cylinder taken to be 1. Those distances are chosen based on the studies of [Sohankar, Norberg, and Davidson (1998); Turki, Abbassi, and Nasrallah (2003); Bouaziz, Kessentini, and Turki (2010)].

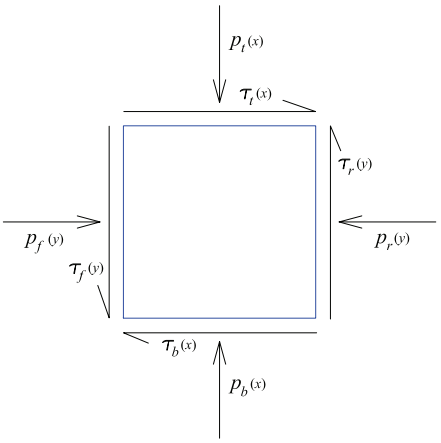

Figure 4: Pressure and shear stress acting on the surface of a square cylinder.

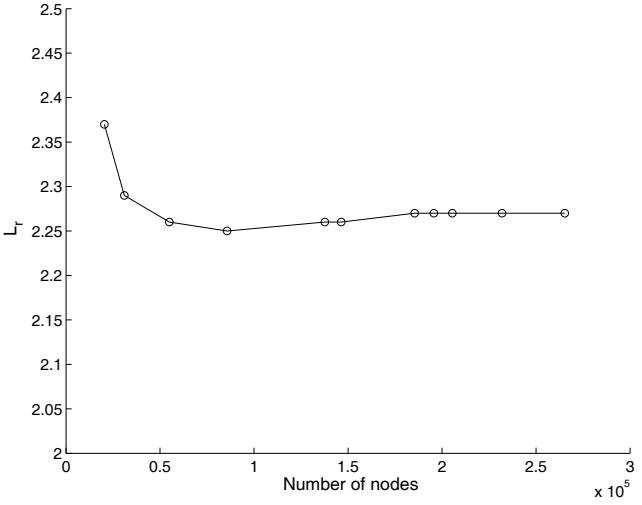

Figure 5: Steady flow past a square cylinder in a channel: grid convergence study of recirculation length L_r for $Re = 40$.

A fully developed laminar flow is assumed at the inlet, thus the inlet velocity is described by a parabolic profile as follows.

$$u = u_{\max}\left(1 - \left(\frac{2y}{H}\right)^2\right) \tag{19}$$

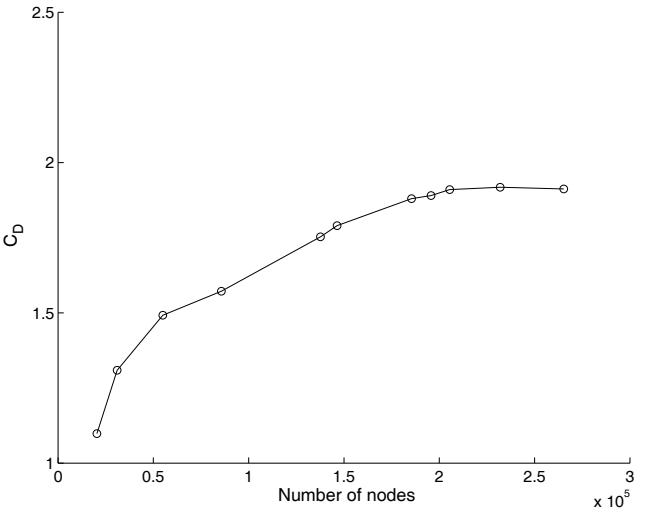

Figure 6: Steady flow past a square cylinder in a channel: grid convergence study of drag coefficient C_D for $Re = 40$.

where u_{max} the maximum velocity at the inlet taken to be 1; and H the height of the channel. The stream function values at the top and bottom walls of the channel (ψ_t and ψ_b) can be determined through Equations 7, 8 and 19. When solving fluid flow problems involving the vortex shedding, the proper boundary condition at the outlet is a very important issue. A suitable outflow boundary condition allows the flow to exit the domain smoothly and has a minimum effect on the behaviour of the flow field. In the present study, the Neumann boundary conditions of the stream function and vorticity at the outlet are considered. It is noted that the value of stream function on the cylinder wall (ψ_w) is equal to zero for the case of steady flows, but is is unknown for the case of unsteady flows. This value ψ_w varies with respect to time and can be determined by using a single-valued pressure condition [Lewis (1979); Le-Cao, Mai-Duy, Tran, and Tran-Cong (2011)].

The non-overlapping domain decomposition technique [Quarteroni and Valli (1999)] is employed here in order to reduce the size of memory required. The continuity of the stream function and vorticity variables and their first-order derivatives are imposed at the subdomain interfaces. The computational domain is decomposed into 24 subdomains. Each subdomain is represented by a uniform Cartesian grid as shown in Fig. 3. Fine grids are generated in the domains near the cylinder in order to obtain reliable and accurate numerical results.

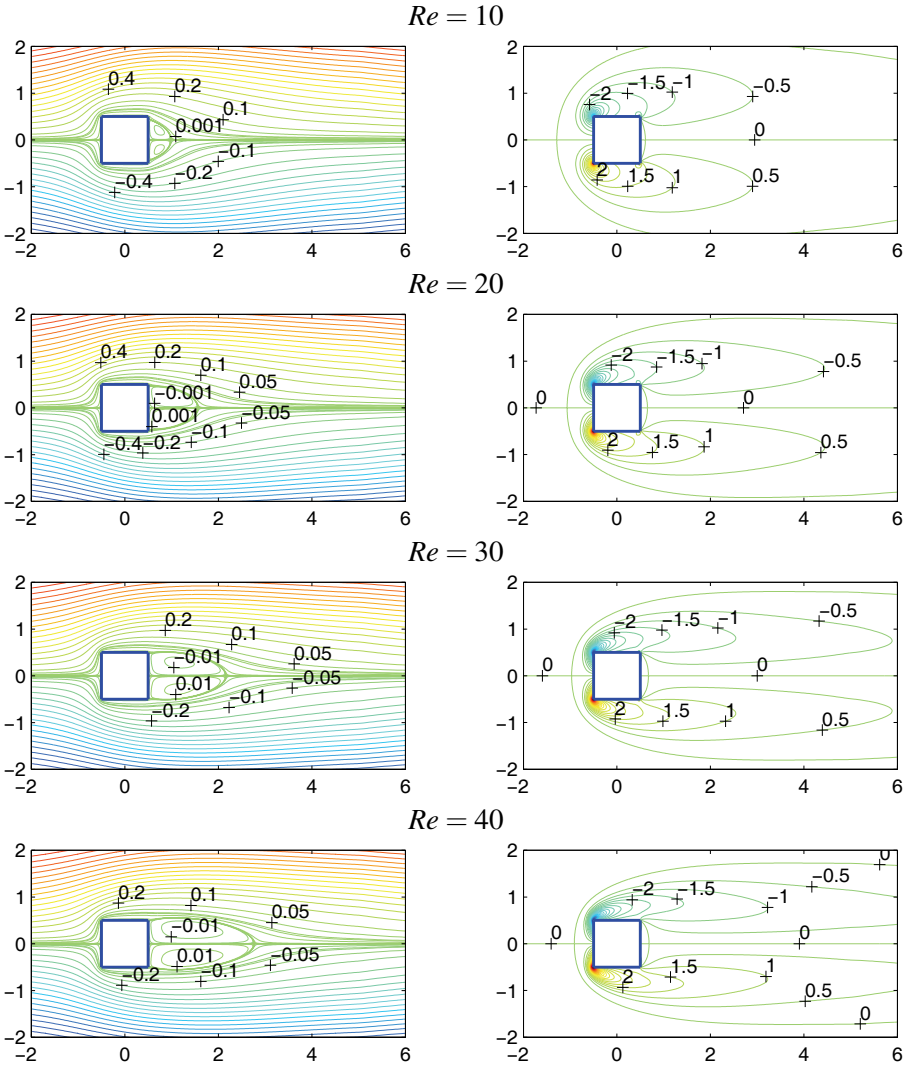

Figure 7: Steady flow past a square cylinder in a channel: contours of stream function for different Reynolds numbers, using a grid of 571×351.

Calculation of drag and lift coefficients

From the primitive variable formulation, the pressure gradients $(\partial p/\partial x, \partial p/\partial y)$ on the square cylinder are given by

$$\frac{\partial p}{\partial x} = \frac{1}{\mathrm{Re}}\left(\frac{\partial^2 u}{\partial x^2} + \frac{\partial^2 u}{\partial y^2}\right) - \left(u\frac{\partial u}{\partial x} + v\frac{\partial u}{\partial x}\right), \tag{20}$$

$$\frac{\partial p}{\partial y} = \frac{1}{\mathrm{Re}}\left(\frac{\partial^2 v}{\partial x^2} + \frac{\partial^2 v}{\partial y^2}\right) - \left(u\frac{\partial v}{\partial x} + v\frac{\partial v}{\partial x}\right), \tag{21}$$

where Re is Reynolds number defined by $Re = u_{max}D/\nu$, D the side length of the square cylinder, ν the kinematic viscosity. For the case of stationary cylinder, the convection terms are equal to zero on the cylinder surface, equations (20) and (21) then become

$$\frac{\partial p}{\partial x} = \frac{1}{Re}\left(\frac{\partial^2 u}{\partial x^2} + \frac{\partial^2 u}{\partial y^2}\right), \tag{22}$$

$$\frac{\partial p}{\partial y} = \frac{1}{Re}\left(\frac{\partial^2 v}{\partial x^2} + \frac{\partial^2 v}{\partial y^2}\right). \tag{23}$$

The vorticity can be determined as

$$\omega = \frac{\partial v}{\partial x} - \frac{\partial u}{\partial y}. \tag{24}$$

Making use of (24) along the top and the bottom of the square cylinder and differentiating both sides with respect to y result in

$$\frac{\partial \omega}{\partial y} = -\frac{\partial^2 u}{\partial y^2}. \tag{25}$$

From Equations (22) and (25), the gradients of pressure along the bottom and the top walls are determined as

$$\frac{\partial p}{\partial x} = -\frac{1}{\mathrm{Re}}\frac{\partial \omega}{\partial y}. \tag{26}$$

In a similar fashion, one can calculate the gradients of pressure along the front and the rear walls as follows.

$$\frac{\partial p}{\partial y} = \frac{1}{\mathrm{Re}}\frac{\partial \omega}{\partial x}. \tag{27}$$

Integrating equations (26) and (27) along the horizontal and vertical walls, respectively, the pressure distribution on the cylinder surface can be determined.

Drag and lift coefficients can be determined as

$$C_D = \frac{F_D}{1/2\rho u_{\max}^2 D}, \tag{28}$$

$$C_L = \frac{F_L}{1/2\rho u_{\max}^2 D}, \tag{29}$$

where ρ is fluid density, and the drag F_D and lift F_L are defined by

$$F_D = F_{D_p} + F_{D_f}, \tag{30}$$

$$F_L = F_{L_p} + F_{L_f}, \tag{31}$$

in which

$$F_{D_p} = \int_0^1 (p_f - p_r)dy, \tag{32}$$

$$F_{L_p} = \int_0^1 (p_b - p_t)dx, \tag{33}$$

$$F_{D_f} = \int_0^1 (\tau_t - \tau_b)dx, \tag{34}$$

$$F_{L_f} = \int_0^1 (\tau_r - \tau_f)dy, \tag{35}$$

where p_f, p_r, p_b, and p_t are values of pressure distribution on the front, rear, bottom and top surfaces of the square cylinder, respectively; and τ_f, τ_r, τ_b, and τ_t are values of shear stress acting on the front, rear, bottom and top surfaces of the square cylinder, respectively, as shown in Fig. 4.

4.2.1 Steady case

A grid independence study for flow past a square cylinder in a channel at Reynolds number of 40 is conducted. The length of recirculation zone L_r and drag coefficient C_D for various grid sizes are presented in Tab. 7. The variations of L_r and C_D with respect to the number of nodes are described in Figs. 5 and 6. It can be seen that the numerical results are convergent with increasing grid density. The flow parameters L_r and C_D for different Reynolds numbers ($Re \leq 40$) using a grid of 571×351 are provided in Tab. 8. The present numerical results are in good agreement with the published results of other authors. Contours of stream function and vorticity of

Table 7: Steady flow past a square cylinder in a channel: grid convergence study of recirculation length L_r and drag coefficient C_D for $Re = 40$.

Grid	L_r	C_D
173×121	2.37	1.10
211×151	2.29	1.31
281×201	2.26	1.49
351×251	2.25	1.57
469×301	2.25	1.75
493×305	2.25	1.79
557×341	2.27	1.88
571×351	2.27	1.89
599×351	2.27	1.91
645×367	2.27	1.92
717×377	2.27	1.91
Breuer, Bernsdorf, Zeiser, and Durst (2000)	2.15	1.70
Gupta, Sharma, Chhabra, and Eswaran (2003)	1.90	1.86
Dhiman, Chhabra, and Eswaran (2005)	2.17	1.75

the flow field around the square cylinder for small Reynolds numbers are given in Fig. 7. It appears that the flow separation occurs at the trailing edges of the cylinder and a closed steady recirculation region containing two symmetric vortices forms behind the cylinder. The size of the recirculation region increases with increasing Reynolds number.

4.2.2 Unsteady case

When the Reynolds number reaches a certain critical value, flow past a square cylinder in a channel becomes unsteady. The critical Reynolds number is a function of the blockage ratio defined in Fig. 2. Here we do not attempt to search for these critical Reynolds numbers and simply investigate the flow for several values of β_0 (1/2, 1/4, and 1/8) and Reynolds numbers ($60 \leq Re \leq 160$). The Strouhal number is calculated based on the frequency of the vortex shedding f, the cylinder length D and the maximum inlet velocity u_{max} as follows.

$$St = \frac{fD}{u_{\max}}. \tag{36}$$

Table 8: Steady flow past a square cylinder in a channel: comparison of recirculation length L_r and drag coefficient C_D, using a grid of 571×351.

Re	Source	L_{sep}	C_D
10	Breuer, Bernsdorf, Zeiser, and Durst (2000)	0.49	3.64
	Gupta, Sharma, Chhabra, and Eswaran (2003)	0.40	3.51
	Dhiman, Chhabra, and Eswaran (2005)	0.49	3.63
	Present	0.48	3.73
20	Breuer, Bernsdorf, Zeiser, and Durst (2000)	1.04	2.50
	Gupta, Sharma, Chhabra, and Eswaran (2003)	0.90	2.45
	Dhiman, Chhabra, and Eswaran (2005)	1.05	2.44
	Present	1.06	2.64
30	Breuer, Bernsdorf, Zeiser, and Durst (2000)	1.60	2.00
	Gupta, Sharma, Chhabra, and Eswaran (2003)	1.40	2.06
	Dhiman, Chhabra, and Eswaran (2005)	1.62	1.99
	Present	1.66	2.15
40	Breuer, Bernsdorf, Zeiser, and Durst (2000)	2.15	1.70
	Gupta, Sharma, Chhabra, and Eswaran (2003)	1.90	1.86
	Dhiman, Chhabra, and Eswaran (2005)	2.17	1.75
	Present	2.27	1.89

Time-averaged drag coefficient C_{Dm} is defined by

$$C_{Dm} = \frac{1}{t_2 - t_1} \int_{t_1}^{t_2} C_D dt, \tag{37}$$

where $t_2 - t_1$ is the period of the vortex shedding.

Figs. 8 and 9 respectively present variations of Strouhal number *St* and time-averaged drag coefficient C_{Dm} with respect to Reynolds number for the case of blockage ratio of $1/8$ and using different grids of 547×331, 571×351 and 645×367. The obtained numerical results are compared with the results of FVM [Breuer, Bernsdorf, Zeiser, and Durst (2000)] both using a non-uniform grid of 560×340, lattice-Boltzmann automata (LBA) method [Breuer, Bernsdorf, Zeiser, and Durst (2000)] using a uniform grid of 2000×320, space-time adaptive method (STAM) [Berrone and Marro (2009)] and control volume finite element method (CVFEM) [Bouaziz, Kessentini, and Turki (2010)] using a non-uniform grid of 249×197. It can be seen that the present numerical results at three different grids are slightly different and in good agreement with the results of other methods. Fig. 10 shows variations of drag

and lift coefficients with respect to time t for the case of $Re = 90$, $\beta_0 = 1/8$ and using a grid of 571×351. It can be seen that those coefficients vary periodically after a certain time. The contours of stream function and vorticity for different Reynolds numbers ($Re = 40, 60, 90$ and 160) and $\beta_0 = 1/8$ are depicted in Figs. 11 and 12, respectively. The well-known von Karman vortices generate behind the cylinder periodically when a critical Reynolds number ($Re \approx 60$) is exceeded.

Table 9: Unsteady flow past a square cylinder in a channel: Strouhal number St and time-averaged drag coefficient C_{Dm} for different blockage ratios $\beta_0 = 1/2, 1/4$ and $1/8$, using grids of 645×191, 645×271 and 645×367, respectively. Note that in the case of $\beta_0 = 1/2,\ 1/4$, the flow is still steady for $Re = 60,\ 80$

	$\beta_0 = 1/2$		$\beta_0 = 1/4$		$\beta_0 = 1/8$	
Re	St	C_{Dm}	St	C_{Dm}	St	C_{Dm}
60	-	7.522	-	1.871	0.122	1.585
80	-	6.237	-	1.634	0.131	1.477
100	0.344	5.396	0.185	1.483	0.137	1.412
120	0.349	4.773	0.192	1.382	0.142	1.366
140	0.352	4.269	0.196	1.303	0.146	1.340
160	0.352	3.850	0.197	1.239	0.148	1.315

Table 10: Unsteady flow past a circular cylinder: Strouhal number St for different Reynolds number $Re = 80, 100$ and 200.

Source	$Re = 80$	$Re = 100$	$Re = 200$
Braza, Chassaing, and Ha-Minh (1986)	-	0.16	0.20
Liu, Zheng, and Sung (1998)	-	0.165	0.192
Ding, Shu, Yeo, and Xu (2004)	-	0.164	0.196
Park, Kwon, and Choi (1998)	0.152	0.165	-
Silva, Silveira-Neto, and Damasceno (2003)	0.15	0.16	-
Present, 548×379	0.159	0.168	-
Present, 640×379	0.151	0.168	0.199

Tab. 9 presents Strouhal number St and time-averaged drag coefficient C_{Dm} for several Reynolds numbers ($60 \leq Re \leq 160$) and blockage ratios ($\beta_0 = 1/2, 1/4$ and

Table 11: Unsteady flow past a circular cylinder: Drag coefficient C_D for different Reynolds number $Re = 80, 100$ and 200.

Source	$Re = 80$	$Re = 100$	$Re = 200$
Braza, Chassaing, and Ha-Minh (1986)	-	1.364 ± 0.015	1.40 ± 0.05
Liu, Zheng, and Sung (1998)	-	1.350 ± 0.012	1.310 ± 0.049
Ding, Shu, Yeo, and Xu (2004)	-	1.325 ± 0.008	1.327 ± 0.045
Park, Kwon, and Choi (1998)	1.35	1.33	-
Silva, Silveira-Neto, and Damasceno (2003)	1.4	1.39	-
Present, 548×379	1.364 ± 0.004	1.344 ± 0.012	-
Present, 640×379	1.365 ± 0.005	1.344 ± 0.012	1.295 ± 0.048

Table 12: Unsteady flow past a circular cylinder: Lift coefficient C_L for different Reynolds number $Re = 80, 100$ and 200.

Source	$Re = 80$	$Re = 100$	$Re = 200$
Braza, Chassaing, and Ha-Minh (1986)	-	± 0.25	± 0.75
Liu, Zheng, and Sung (1998)	-	± 0.339	± 0.69
Ding, Shu, Yeo, and Xu (2004)	-	± 0.28	± 0.60
Park, Kwon, and Choi (1998)	± 0.245	± 0.332	-
Silva, Silveira-Neto, and Damasceno (2003)	± 0.235	-	-
Present, 548×379	± 0.237	± 0.344	-
Present, 640×379	± 0.245	± 0.341	± 0.70

$1/8$). It is noted that in the cases of $\beta_0 = 1/2$ and $1/4$, the flow is still steady for $Re = 60$ and 80. The influences of Reynolds number on the Strouhal number St and time-averaged drag coefficient C_{Dm} for blockage ratios ($\beta_0 = 1/2$ and $1/4$) are described in Figs. 13 and 14, respectively. It can be seen that Reynolds number has a very weak influence on the Strouhal number for those cases, and the time-averaged drag coefficient decreases with increasing Reynolds number up to 160. Figs. 15 and 16 presents the contours of stream function and vorticity of flow field around the square cylinder in a channel with blockage ratio of $1/4$, while the corresponding contours for the case of blockage ratio of $1/2$ are given in Figs. 17 and 18. Figs. 11, 15 and 17 indicate that the critical Reynolds number (at which the flow becomes unsteady) increases with increasing blockage ratio. For example, at $Re = 60$, the flow becomes unsteady in the case of $\beta_0 = 1/8$, but is still steady in the case of $\beta_0 = 1/4$. At $Re = 100$, the flow becomes unsteady in the case of

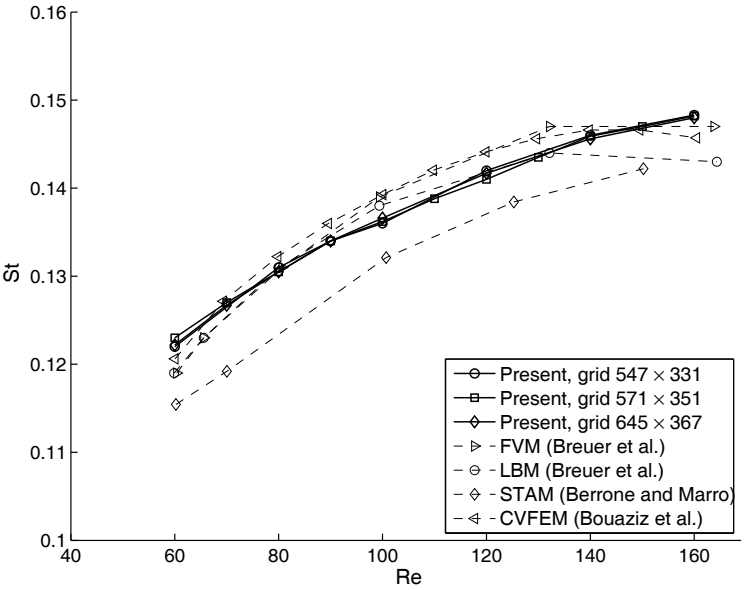

Figure 8: Unsteady flow past a square cylinder in a channel (blockage ratio $\beta_0 = 1/8$): variation of Strouhal number St with respect to Reynolds number Re, using different grids of 547×331, 571×351 and 645×367; FVM [Breuer, Bernsdorf, Zeiser, and Durst (2000)] using a non-uniform grid of 560×340; LBA [Breuer, Bernsdorf, Zeiser, and Durst (2000)] using a uniform grid of 2000×320; STAM [Berrone and Marro (2009)]; CVFEM [Bouaziz, Kessentini, and Turki (2010)] using a non-uniform grid of 249×197.

$\beta_0 = 1/4$, but remains nearly steady in the case of $\beta_0 = 1/2$. The numerical results obtained are in good agreement with those of Sahu, Chhabra, and Eswaran (2010) who used the semi-explicit FEM.

4.3 Example 3: Unsteady flows past a circular cylinder

The unsteady flow past a circular cylinder at different Reynolds numbers ($Re = 80, 100$ and 200) is considered here, where $Re = U_0 D/\nu$, U_0 is the far-field inlet velocity taken to be 1, D the diameter of the cylinder taken to be 1, ν the kinematic viscosity. The same numerical procedure as in Example 2 is employed. The problem geometry and boundary conditions are described in Fig. 19. Note that computational boundary conditions for vorticity are determined by Equations (9)-(13). The computational domain is decomposed into 25 subdomains as shown in

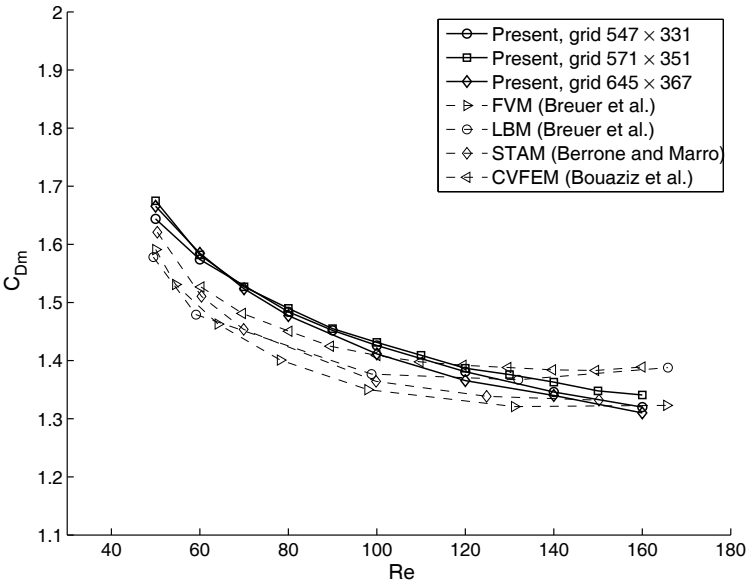

Figure 9: Unsteady flow past a square cylinder in a channel (blockage ratio $\beta_0 = 1/8$): variation of time-averaged drag coefficient C_{Dm} with respect to Reynolds number Re, using different grids of 547×331, 571×351 and 645×367; FVM [Breuer, Bernsdorf, Zeiser, and Durst (2000)] using a non-uniform grid of 560×340; LBA [Breuer, Bernsdorf, Zeiser, and Durst (2000)] using a uniform grid of 2000×320; STAM [Berrone and Marro (2009)]; CVFEM [Bouaziz, Kessentini, and Turki (2010)] using a non-uniform grid of 249×197.

Fig. 20. A finer grid is generated in the subdomain containing the circular cylinder. The far-field flow is assumed to behave as a potential flow and the far-field stream function ψ^{far} can be defined by [Kim, Kim, Jun, and Lee (2007)]

$$\psi^{far} = U_0 y \left(1 - \frac{D^2}{4(x^2+y^2)}\right). \tag{38}$$

The boundary conditions for stream function are given by

$$\psi = \psi^{far},\ \omega = 0, \qquad \text{on } \Gamma_1, \Gamma_2, \Gamma_3 \tag{39}$$

$$\frac{\partial \psi}{\partial x} = 0,\ \frac{\partial \omega}{\partial x} = 0, \qquad \text{on } \Gamma_4 \tag{40}$$

$$\psi = \psi_w, \frac{\partial \psi}{\partial n} = 0, \qquad \text{on } \Gamma_w \tag{41}$$

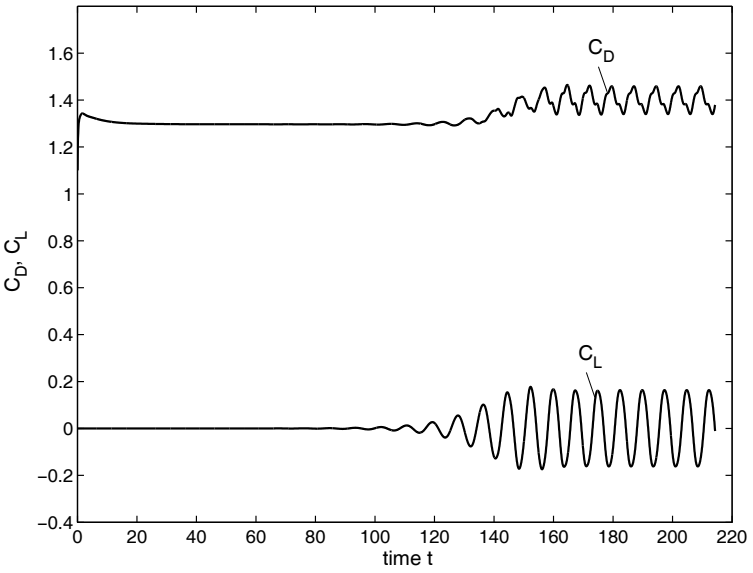

Figure 10: Unsteady flow past a square cylinder in a channel (blockage ratio $\beta_0 = 1/8$): variation of drag coefficient C_D and lift coefficient C_L with respect to time t for the case of $Re = 90$, using a grid of 571×351.

where n is the direction normal to the cylinder surface; ψ_w the unknown stream function value on the cylinder wall, Γ_w; and the subscript w is used to denote quantities on Γ_w. The value ψ_w varies with respect to time and can be determined by using a single-valued pressure condition [Lewis (1979); Le-Cao, Mai-Duy, Tran, and Tran-Cong (2011)].

Tabs. 10-12 respectively present Strouhal number, drag and lift coefficients for different Reynolds numbers. The present numerical results are in good agreement with the published results of other authors. Fig. 21 presents the variations of drag and lift coefficients with respect to time for $Re = 100$. The periodic variations of these coefficients are observed as time goes on. The contours of stream function and vorticity of the flow field around the circular cylinder at different Reynolds numbers are provided in Figs. 22 and 23, respectively. With increasing Reynolds number, the vortex shedding frequency increases and the vortices become smaller.

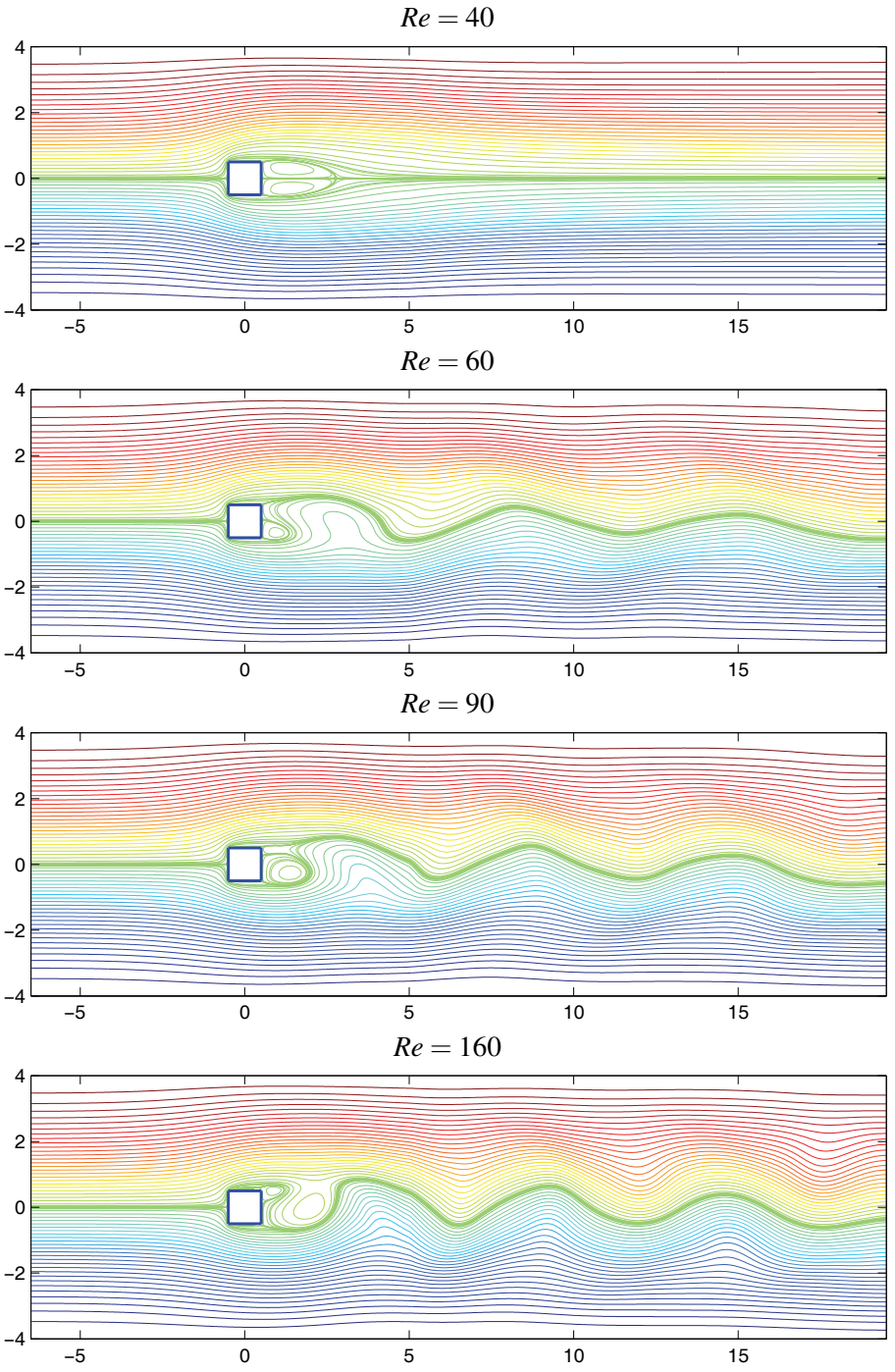

Figure 11: Unsteady flow past a square cylinder in a channel (blockage ratio $\beta_0 = 1/8$): Contours of stream function for different Reynolds numbers, using a grid of 645×367.

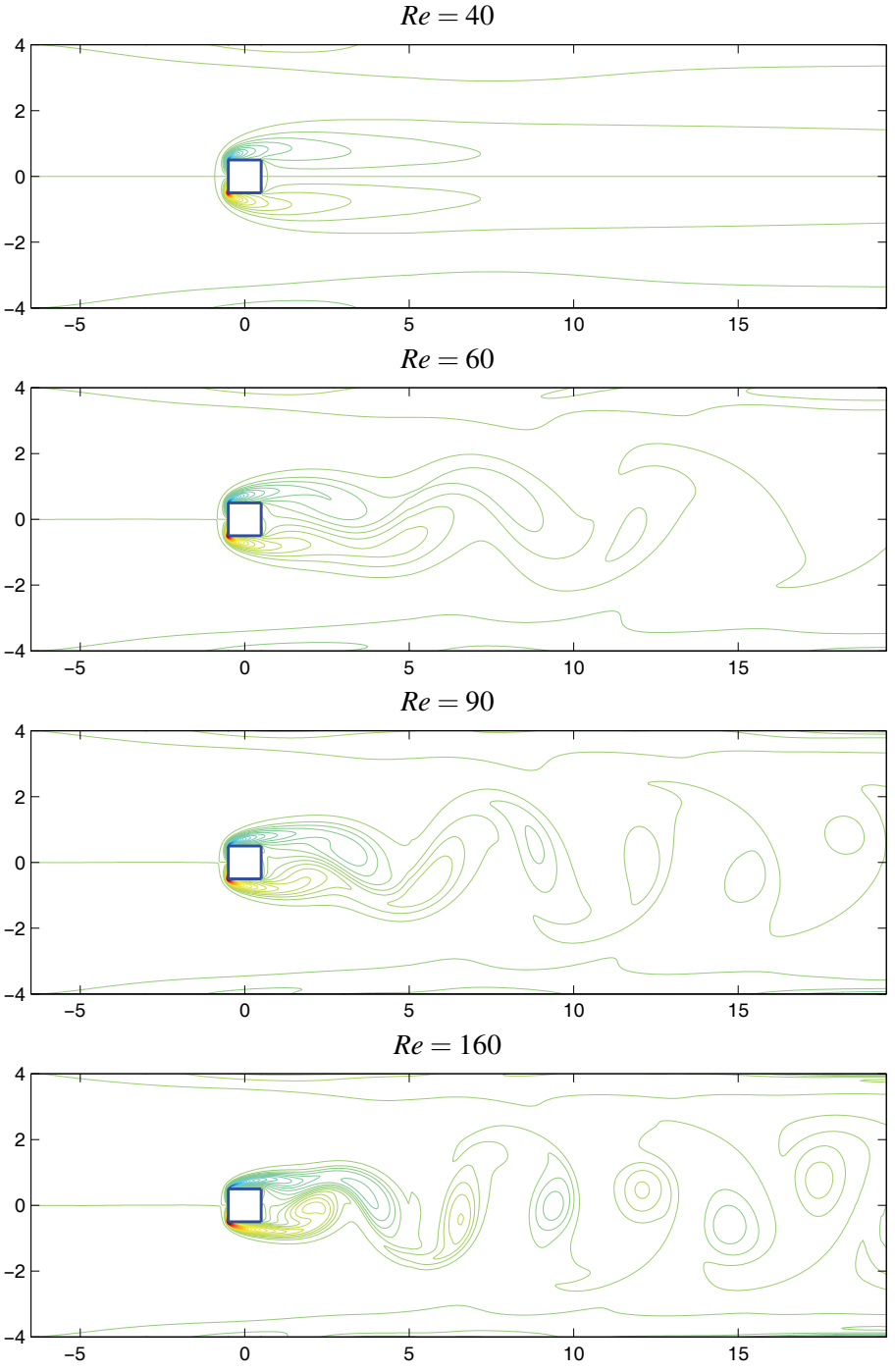

Figure 12: Unsteady flow past a square cylinder in a channel (blockage ratio $\beta_0 = 1/8$): Contours of vorticity for different Reynolds numbers, using a grid of 645×367.

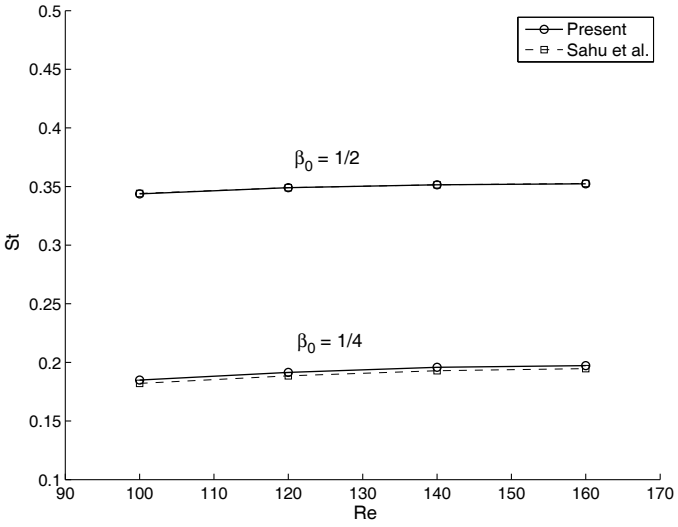

Figure 13: Unsteady flow past a square cylinder in a channel: variation of time-averaged drag coefficient C_{Dm} with respect to Reynolds number *Re* for blockage ratios $\beta_0 = 1/2$ and $1/4$, using grids of 645×191 and 645×271, respectively.

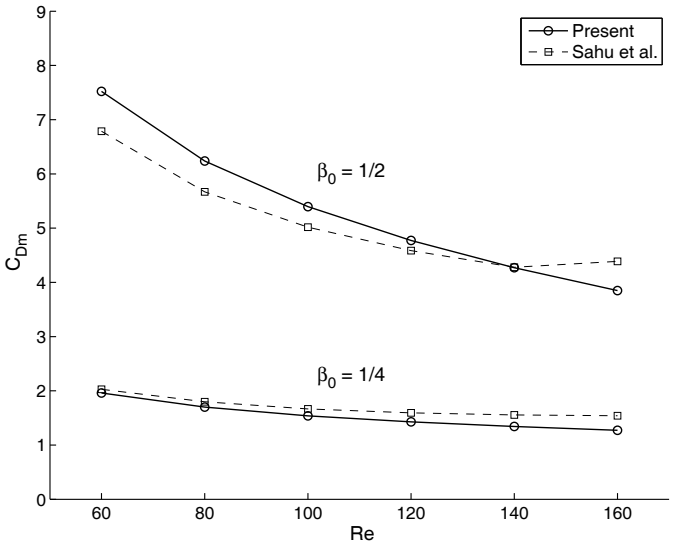

Figure 14: Unsteady flow past a square cylinder in a channel: variation of time-averaged drag coefficient C_{Dm} with respect to Reynolds number *Re* for blockage ratios $\beta_0 = 1/2$ and $1/4$, using grids of 645×191 and 645×271, respectively.

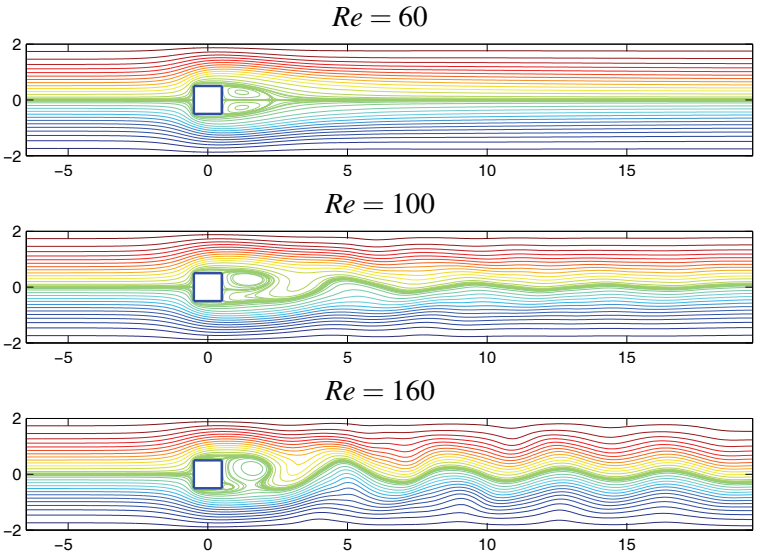

Figure 15: Unsteady flow past a square cylinder in a channel: Contours of stream function for different Reynolds numbers ($\beta_0 = 1/4$, grid = 645×271).

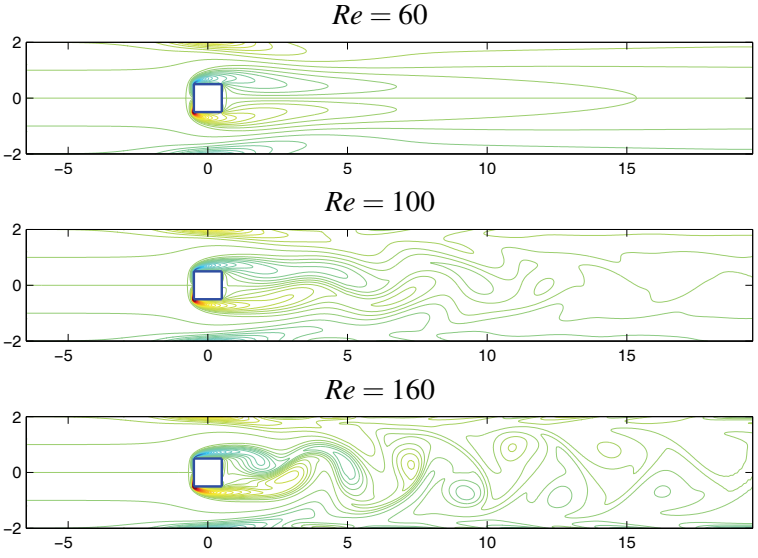

Figure 16: Unsteady flow past a square cylinder in a channel: Contours of vorticity for different Reynolds numbers ($\beta_0 = 1/4$, grid = 645×271).

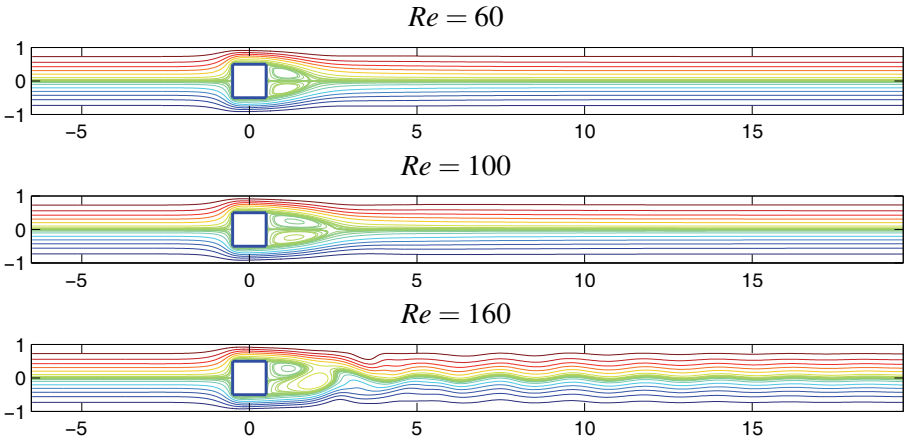

Figure 17: Unsteady flow past a square cylinder in a channel: Contours of stream function for different Reynolds numbers ($\beta_0 = 1/2$, grid = 645×191).

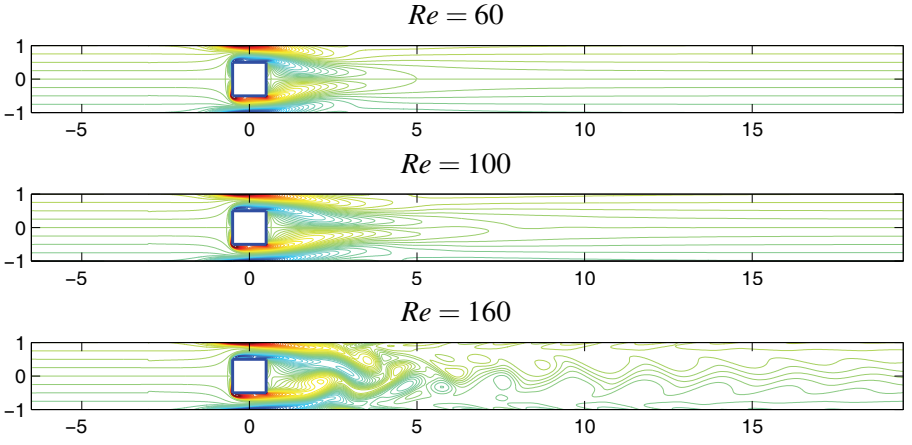

Figure 18: Unsteady flow past a square cylinder in a channel: Contours of vorticity for different Reynolds numbers ($\beta_0 = 1/2$, grid = 645×191).

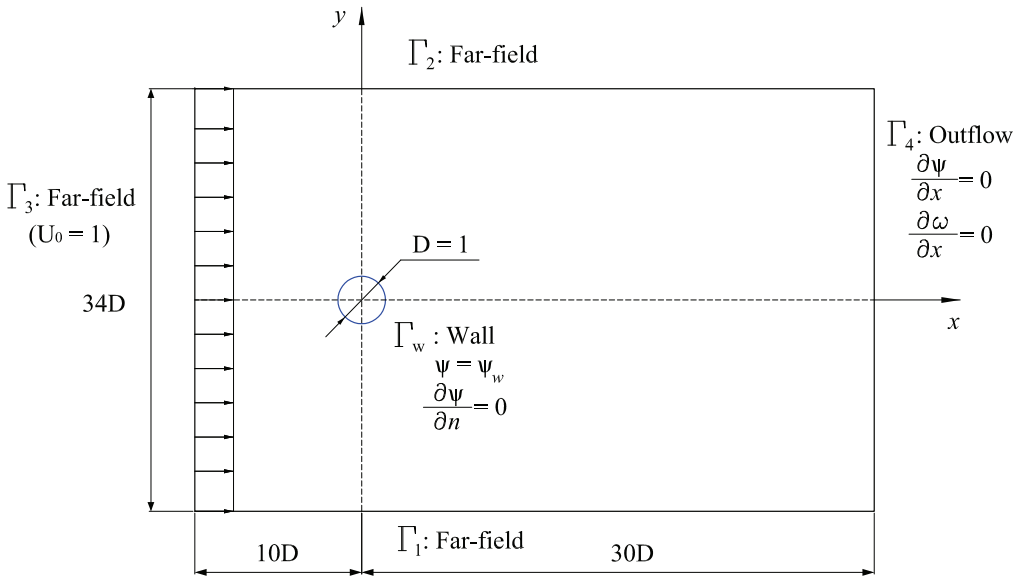

Figure 19: Unsteady flow past a circular cylinder: geometry and boundary conditions. Note that computational boundary conditions for vorticity are determined by Equations (9)-(13).

5 Conclusions

A new numerical procedure based on the local MLS-1D-IRBFN method is presented for time-dependent problems. The numerical results for Burgers' equation indicate that the LMLS-1D-IRBFN approach yields the same level of accuracy as the 1D-IRBFN method, while the system matrix is more sparse than that of the 1D-IRBFN, which helps reduce the computational cost significantly. The LMLS-1D-IRBFN shape function possesses the Kronecker-δ property which allows an exact imposition of the essential boundary condition. Cartesian grids are employed to discretise both regular and irregular problem domains. The combination of the present numerical procedure and a domain decomposition technique is successfully developed for simulating steady and unsteady flows past a square cylinder in a horizontal channel with different blockage ratios and unsteady flows past a circular cylinder. The influence of blockage ratio on the characteristics of flow past a square cylinder in a channel is investigated for a range of Reynolds numbers ($60 \leq Re \leq 160$) and several blockage ratios ($\beta_0 = 1/2, 1/4$ and $1/8$). The obtained numerical results indicate that (i) the critical Reynolds number (at which

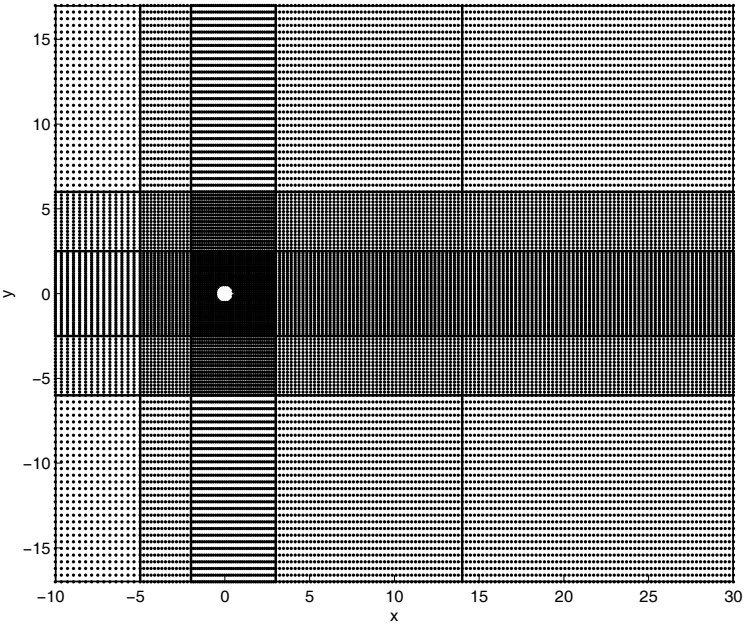

Figure 20: Unsteady flow past a circular cylinder: grid configuration.

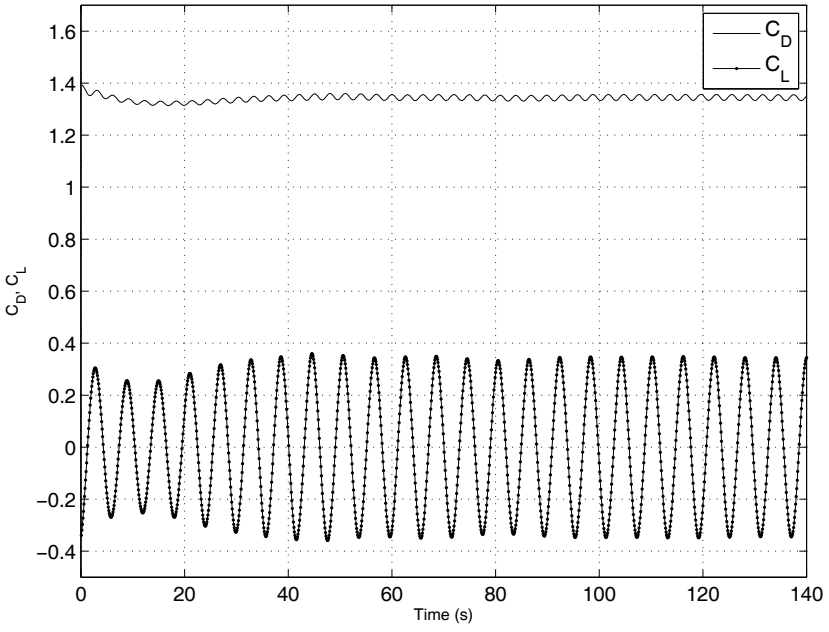

Figure 21: Unsteady flow past a stationary cylinder: drag and lift coefficients C_D and C_L with respect to time for $Re = 100$, using a grid of 548×379.

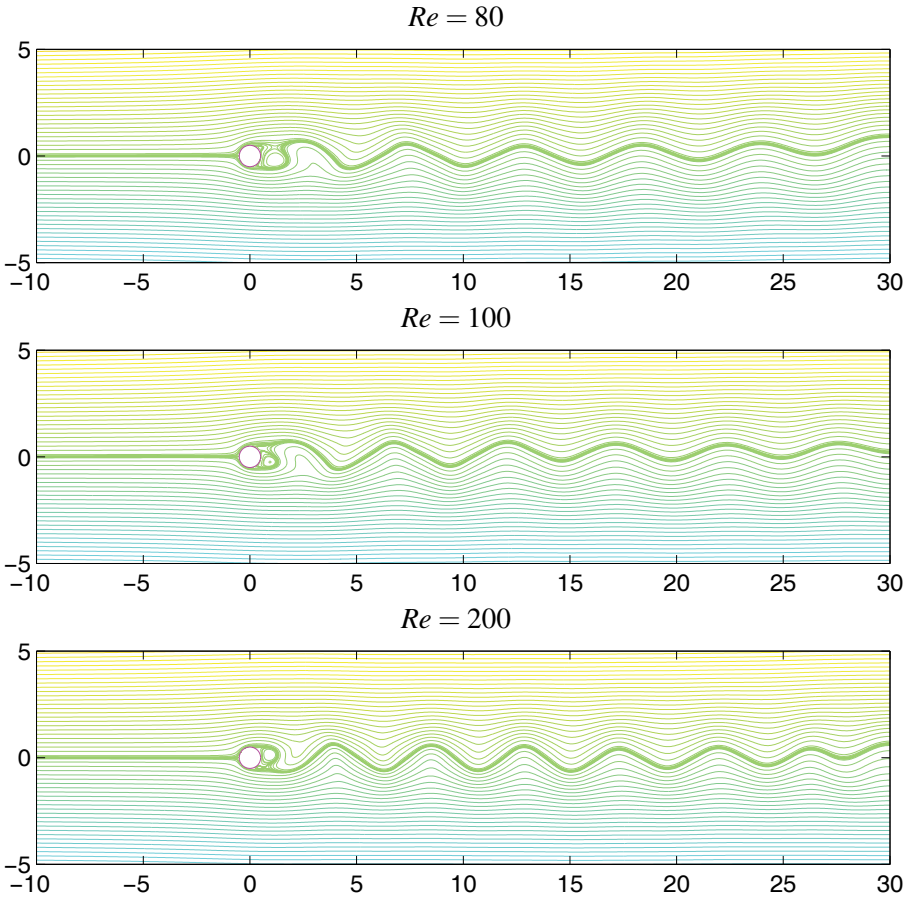

Figure 22: Unsteady flow past a circular cylinder: contours of stream function for different Reynolds numbers $Re = 80, 100$ and 200, using grids of 548×379, 548×379 and 640×379, respectively.

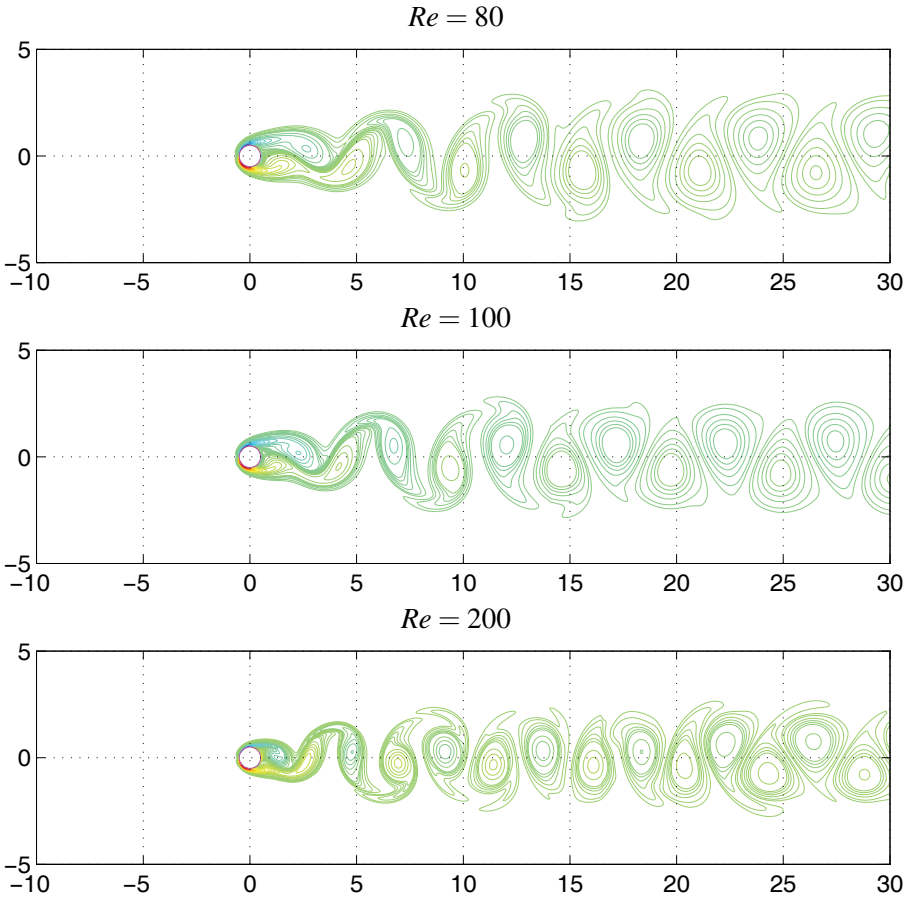

Figure 23: Unsteady flow past a circular cylinder: contours of vorticity for different Reynolds numbers $Re = 80, 100$ and 200, using grids of 548×379, 548×379 and 640×379, respectively.

the flow becomes unsteady) increases with increasing blockage ratio; (ii) time-averaged drag coefficient decreases with increasing Reynolds number up to 160; and (iii) the Reynolds number has a very weak influence on the Strouhal number for the cases of $\beta_0 = 1/2$ and $1/4$.

Acknowledgement: This research is supported by the University of Southern Queensland, Australia through a USQ Postgraduate Research Scholarship awarded to D. Ngo-Cong.

References

Babuŝka, I.; Melenk, J. M. (1997): The partition of unity method. *International Journal for Numerical Methods in Engineering*, vol. 40, pp. 727–758.

Berrone, S.; Marro, M. (2009): Sapce-time adaptive simulations for unsteady Navier-Stokes problems. *Computers & Fluids*, vol. 38, pp. 1132–1144.

Bouaziz, M.; Kessentini, S.; Turki, S. (2010): Numerical prediction of flow and heat transfer of power-law fluids in a plane channel with a built-in heated square cylinder. *International Journal of Heat and Mass Transfer*, vol. 53, pp. 5420–5429.

Braza, M.; Chassaing, P.; Ha-Minh, H. (1986): Numerical study and physical analysis of the pressure and velocity fields in the near wake of a circular cylinder. *The Journal of Fluid Mechanics*, vol. 165, pp. 79–130.

Breuer, M.; Bernsdorf, J.; Zeiser, T.; Durst, F. (2000): Accurate computations of the laminar flow past a square cylinder based on two different methods: lattice-Boltzmann and finite-volume. *International Journal of Heat and Fluid Flow*, vol. 21, pp. 186–196.

Caldwell, J.; Wanless, P.; Cook, A. E. (1987): Solution of Burgers' equation for large Reynolds number using finite elements with moving nodes. *Applied Mathematical Modelling*, vol. 11, pp. 211–227.

Chen, J. S.; Hu, W.; Hu, H. Y. (2008): Reproducing kernel enhanced local radial basis collocation method. *International Journal for Numerical Methods in Engineering*, vol. 75, pp. 600–627.

Cheng, M.; Liu, G. R.; Lam, K. Y. (2001): Numerical simulation of flow past a rotationally oscillating cylinder. *Computer & Fluids*, vol. 30, pp. 365–392.

Cole, J. D. (1951): On a quasi-linear parabolic equation occuring in aerodynamics. *Quarterly Journal of Applied Mathematics*, vol. 9, pp. 225–236.

Davis, R. W.; Moore, E. F. (1982): A numerical study of vortex shedding from rectangles. *The Journal of Fluid Mechanics*, vol. 116, pp. 475–506.

Dhiman, A. K.; Chhabra, R. P.; Eswaran, V. (2005): Flow and heat transfer across a confined square cylinder in the steady flow regime: Effect of Peclet number. *International Journal of Heat and Mass Transfer*, vol. 48, pp. 4598–4614.

Dhiman, A. K.; Chhabra, R. P.; Eswaran, V. (2008): Steady mixed convection across a confined square cylinder. *International Communications in Heat and Mass Transfer*, vol. 35, pp. 47–55.

Ding, H.; Shu, C.; Yeo, K. S.; Xu, D. (2004): Simulation of incompressible viscous flows past a circular cylinder by hybrid FD scheme and meshless least square-based finite difference method. *Computer Methods in Applied Mechanics and Engineering*, vol. 193, pp. 727–744.

Ding, H.; Shu, C.; Yeo, K. S.; Xu, D. (2007): Numerical simulation of flows around two circular cylinders by mesh-free least square-based finite difference methods. *International Journal for Numerical Methods in Fluids*, vol. 53, pp. 305–332.

Gupta, A. K.; Sharma, A.; Chhabra, R. P.; Eswaran, V. (2003): Two-dimensional steady flow of a power-law fluid past a square cylinder in a plane channel: Momentum and heat-transfer characteristics. *Industrial & Engineering Chemistry Research*, vol. 42, pp. 5674–5686.

Hashemian, A.; Shodja, H. M. (2008): A meshless approach for solution of Burgers' equation. *Journal of Computational and Applied Mathematics*, vol. 220, pp. 226–239.

Hassanien, I. A.; Salama, A. A.; Hosham, H. A. (2005): Fourth-order finite difference method for solving Burgers' equation. *Applied Mathematics and Computation*, vol. 170, pp. 781–800.

Hon, Y. C.; Mao, X. Z. (1998): An efficient numerical scheme for Burgers' equation. *Applied Mathematics and Computation*, vol. 97, pp. 37–50.

Hosseini, B.; Hashemi, R. (2011): Solution of Burgers' equation using a local-RBF meshless method. *International Journal for Computational Methods in Engineering Science and Mechanics*, vol. 12, pp. 44–58.

Iskander, L.; Mohsen, A. (1992): Some numerical experiments on splitting of Burgers' equation. *Numerical Methods for Partial Differential Equations*, vol. 8, pp. 267–276.

Kansa, E. J. (1990): Multiquadrics - A Scattered Data Approximation Scheme with Applications to Computational Fulid-Dynamics - II: Solutions to parabolic, Hyperbolic and Elliptic Partial Differential Equations. *Computers & Mathematics with Applications*, vol. 19 (8-9), pp. 147–161.

Kim, Y.; Kim, D. W.; Jun, S.; Lee, J. H. (2007): Meshfree point collocation method for the stream-vorticity formulation of 2D incompressible Navier-Stokes equations. *Computer Methods in Applied Mechanics and Engineering*, vol. 196, pp. 3095–3109.

Le, P. B. H.; Rabczuk, T.; Mai-Duy, N.; Tran-Cong, T. (2010): A moving IRBFN-based integration-free meshless method. *CMES: Computer Modeling in Engineering & Sciences*, vol. 61 (1), pp. 63–109.

Le-Cao, K.; Mai-Duy, N.; Tran, C.-D.; Tran-Cong, T. (2011): Numerical study of stream-function formulation governing flows in multiply-connected domains by integrated RBFs and Cartesian grids. *Computers & Fluids*, vol. 44 (1), pp. 32–42.

Le-Cao, K.; Mai-Duy, N.; Tran-Cong, T. (2009): An effective integrated-RBFN Cartesian-grid discretization for the stream function-vorticity-temperature formulation in nonrectangular domains. *Numerical Heat Transfer, Part B*, vol. 55, pp. 480–502.

Lewis, E. (1979): Steady flow between a rotating circular cylinder and fixed square cylinder. *The Journal of Fluid Mechanics*, vol. 95 (3), pp. 497–513.

Liu, C.; Zheng, Z.; Sung, C. H. (1998): Preconditioned multigrid methods for unsteady incompressible flows. *Journal of Computational Physics*, vol. 139, pp. 35–57.

Liu, G. R. (2003): *Meshfree Methods: Moving Beyond the Finite Element Method*. CRC Press, London.

Mai-Duy, N.; Tanner, R. I. (2007): A Collocation Method based on One-Dimensional RBF Interpolation Scheme for Solving PDEs. *International Journal of Numerical Methods for Heat & Fluid Flow*, vol. 17 (2), pp. 165–186.

Mai-Duy, N.; Tran-Cong, T. (2001): Numerical solution of differential equations using multiquadric radial basis function networks. *Neural Networks*, vol. 14, pp. 185–199.

Mai-Duy, N.; Tran-Cong, T. (2001): Numerical Solution of Navier-Stokes Equations using Multiquadric Radial Basis Function Networks. *International Journal for Numerical Methods in Fluids*, vol. 37, pp. 65–86.

Moussaoui, M. A.; Jami, M.; Mezrhab, A.; Naji, H. (2010): MRT-Lattice Bolztmann simulation of forced convection in a plane channel with an inclined square cylinder. *International Journal of Thermal Sciences*, vol. 49, pp. 131–142.

Ngo-Cong, D.; Mai-Duy, N.; Karunasena, W.; Tran-Cong, T. (2011): Free vibration analysis of laminated composite plates based on FSDT using one-dimensional IRBFN method. *Computers & Structures*, vol. 89, pp. 1–13.

Ngo-Cong, D.; Mai-Duy, N.; Karunasena, W.; Tran-Cong, T. (2012): Local Moving Least Square - One-Dimensional IRBFN Technique for Incompressible Viscous Flows. *International Journal for Numerical Methods in Fluids*, pg. (published online 9/Jan/2012 DOI: 10.1002/fld.3640).

Park, J.; Kwon, K.; Choi, H. (1998): Numerical solutions of flow past a circular cylinder at Reynolds numbers up to 160. *KSME International Journal*, vol. 12 (6), pp. 1200–1205.

Quarteroni, A.; Valli, A. (1999): *Domain Decomposition Methods for Partial Differential Equations*. Clarendon Press, Oxford.

Russell, D.; Wang, Z. J. (2003): A Cartesian grid method for modeling multiple moving objects in 2D incompressible viscous flow. *Journal of Computational Physics*, vol. 191, pp. 177–205.

Sahu, A. K.; Chhabra, R. P.; Eswaran, V. (2010): Two-dimensional laminar flow of a power-law fluid across a confined square cylinder. *Journal of Non-Newtonian Fluid Mechanics*, vol. 165, pp. 752–763.

Sanyasiraju, Y. V. S. S.; Chandhini, G. (2008): Local radial basis function based gridfree scheme for unsteady incompressible viscous flows. *Journal of Computational Physics*, vol. 227, pp. 8922–8948.

Shu, C.; Ding, H.; Yeo, K. S. (2003): Local radial basis function-based differential quadrature method and its application to solve two-dimensional incompressible Navier-Stokes equations. *Computer Methods in Applied Mechanics and Engineering*, vol. 192, pp. 941–954.

Shu, C.; Ding, H.; Yeo, K. S. (2005): Computation of Incompressible Navier-Stokes equations by local RBF-based differential quadrature method. *CMES: Computer Modeling in Engineering & Sciences*, vol. 7 (2), pp. 195–205.

Silva, A. L. F. L. E.; Silveira-Neto, A.; Damasceno, J. J. R. (2003): Numerical simulation of two-dimensional flows over a circular cylinder using the immersed boundary method. *Journal of Computational Physics*, vol. 189, pp. 351–370.

Sohankar, A.; Norberg, C.; Davidson, L. (1998): Low-Reynolds-number flow around a square cylinder at incidence: study of blockage, onset of vortex shedding and outlet boundary condition. *International Journal for Numerical Methods in Fluids*, vol. 26, pp. 39–56.

Turki, S.; Abbassi, H.; Nasrallah, S. B. (2003): Two-dimensional laminar fluid flow and heat transfer in a channel with a built-in heated square cylinder. *International Journal of Thermal Sciences*, vol. 42, pp. 1105–1113.

Udaykumar, H. S.; Mittal, R.; Rampunggoon, P.; Khanna, A. (2001): A sharp interface Cartesian grid method for simulating flows with complex moving boundaries. *Journal of Computational Physics*, vol. 174, pp. 345–380.

Vertnik, R.; Šarler, B. (2006): Meshless local radial basis function collocation method for convective-diffusive solid-liquid phase change problems. *International Journal of Numerical Methods for Heat and Fluid Flow*, vol. 16, pp. 617–640.

Zaki, T. G.; Sen, M.; el Hak, M. G. (1994): Numerical and experimental investigation of flow past a freely rotatable square cylinder. *Journal of Fluids and Structures*, vol. 8, pp. 555–582.

Zheng, Z. C.; Zhang, N. (2008): Frequency effects on lift and drag for flow past an oscillating cylinder. *Journal of Fluids and Structures*, vol. 24, pp. 382–399.